

Electric-field Quantum Sensing Exploiting a Photogenerated Charge-transfer Triplet State in a Molecular Semiconductor

Niccoló Fontana,¹ Mikhail V. Vaganov,¹ Gabriel Moise,¹ William K. Myers,² Kun Peng,¹ Arzhang Ardavan,¹ and Junjie Liu^{1,3}

¹*Department of Physics, University of Oxford, The Clarendon Laboratory, Parks Road, Oxford OX1 3PU, UK*

²*CAESR, Inorganic Chemistry Laboratory, University of Oxford, South Parks Road, Oxford OX1 3QR, UK*

³*School of Physical and Chemical Sciences, Queen Mary University of London, London E1 4NS, UK*

Molecular spin systems are promising platforms for quantum sensing due to their chemically tunable Hamiltonians, enabling tailored coherence properties and interactions with external fields. However, electric field sensing remains challenging owing to typically weak spin-electric coupling (SEC) and limited directional sensitivity. Addressing these issues using heavy atoms exhibiting strong atomic spin-orbit couplings (SOC) often compromises spin coherence times. Here, we demonstrate coherent electric field sensing using a photogenerated charge-transfer (CT) spin triplet state in the organic molecule ACRSA (10-phenyl-10H,10'H-spiro[acridine-9,9'-anthracen]-10'-one). By embedding electric field pulses within a Hahn echo sequence, we coherently manipulate the spin triplet and extract both the magnitude and directional dependence of its SEC. The measured SEC strength is approximately 1.20 Hz/(V/m), comparable to values reported in systems with strong atomic SOC, illustrating that heavy atoms are not a prerequisite for electric-field sensitivity of spin states. Our findings position organic CT triplets as chemically versatile and directionally sensitive quantum sensors of E -fields that function without atomic-SOC-mediated mechanisms.

INTRODUCTION

Quantum sensing exploits the unique properties of quantum systems such as quantum coherence and entanglement to achieve unprecedented precision in measuring physical quantities [1]. This paradigm has enabled remarkable advances across diverse platforms, including nitrogen-vacancy centres in diamond [2], superconducting circuits [3], and cold atoms [4]. Quantum sensing of electric fields, in particular, has seen rapid development through systems like Rydberg atoms [5], trapped ions [6], and superconducting circuits [7], which offer excellent sensitivity *via* strong coupling to electric fields. Yet, these platforms typically operate at micrometer to millimeter scales, limiting their spatial resolution and hindering their ability to access electric fields near surfaces or within heterogeneous environments [8, 9].

Molecular electron spins have long been studied as promising candidates for magnetic field sensing due to their well-defined spin states and intrinsic coupling to magnetic fields *via* the Zeeman effect [10]. Another strength lies in the ability to extensively tailor their properties through chemical design, enabling controlled coupling to electric [11], optical [12], and mechanical [13] degrees of freedom, as well as impressively long phase coherence times, up to milliseconds at room temperature [14]. Building on these advantages, recent efforts have begun exploring molecular spins for electric field sensing. Molecular systems offer a compelling route, as their intrinsically nanoscale dimensions enable high spatial resolution and placement in direct proximity to the sensing target [15].

Progress toward electric field sensing with molecular sys-

tems has revealed that molecular spins can exhibit strong coupling to electric fields [16, 17]. However, to achieve sufficient sensitivity using electron spin resonance, a significant spin polarization in magnetically diluted samples is desirable, often necessitating low temperatures. An alternative route to large spin polarisations is offered by light-induced species such as spin-correlated radical pairs (SCRPs), which have shown room-temperature operation, owing to the generation of polarized spin states through spin-selective processes during their formation [18]. SCRPs have been widely investigated as potential candidates for spin qubits, particularly for implementing 2-qubit gates, where two electron spins are correlated *via* zero-field splitting or J-coupling [15]. Quantum teleportation has already been successfully demonstrated using SCRPs, highlighting their ability to embody entangled states between two electron spins within a molecule [19]. Recently, Xie *et al.* [20] demonstrated the use of SCRPs for electric-field sensing by encapsulating a cyclophane host around one of the radical pair partners. In this case, the local supramolecular electric field modulates the inter-spin distance and leads to a different modulation frequency in the out-of-phase component of the spin echo. Crucially, however, such electric field effects on light-induced spin states have, until now, not been demonstrated using externally applied (and controllable) E -fields.

Here, we report the spin-electric coupling (SEC) in a commercially available organic molecular semiconductor spiro-acridine-anthracenone known as ACRSA. Our investigation does not involve structural modifications to the molecule, but instead focuses on detecting externally generated electric fields (and their direction), which alter the system's resonance frequency. This frequency

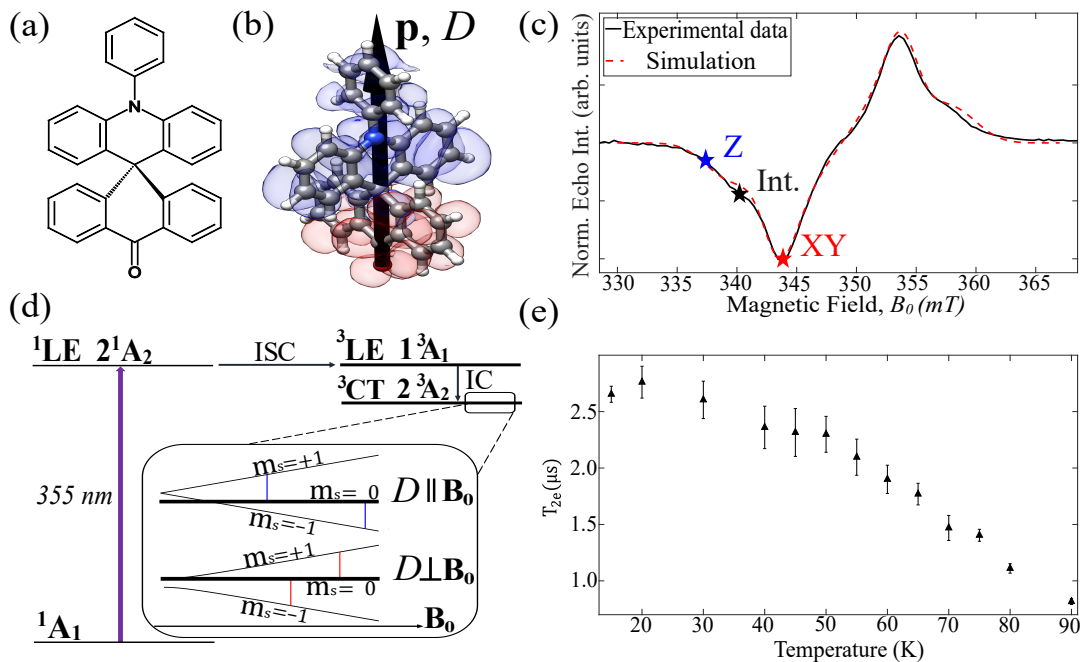


FIG. 1. (a) The schematic molecular structure of ACRSA. (b) The spin density of the charge-transfer triplet state induced by photoexcitation with $\lambda = 355$ nm, computed with the ORCA software (B3LYP/EPR-II basis). The blue (red) molecular orbitals correspond to the lower (higher) singly occupied molecular orbitals, coinciding with the hole (electron) density. The black arrow is the predicted orientation of the longitudinal zero-field splitting tensor/electric dipole moment, and it is defined as the z -axis for the experiment. (c) The (X-band) experimental and simulated field sweep of ACRSA doped into a PMMA matrix ($\sim 90 \mu\text{M}$) at 20 K. The three starred points correspond to the fields where we conducted the spin-electric coupling measurements. (d) Schematic showing the optical pathway that leads to the formation of the triplet charge-transfer state to be electrically modulated, including the initial photoexcitation with $\lambda = 355$ nm, intersystem crossings (ISC), and internal conversion (IC). Inset: The simplified Zeeman energy diagrams when the longitudinal zero-field splitting (D) is parallel (top) and perpendicular (bottom) to the principal magnetic field, together with the allowed ESR transitions. (e) The electronic phase-memory time (T_{2e}) as a function of temperature. T_{2e} exceeds $2.5 \mu\text{s}$ at 20 K, and remains above $1.0 \mu\text{s}$ at 77 K.

shift can be measured using the modified spin-echo sequence first proposed by Mims [21]. Facilitating practical implementation, ACRSA molecules can be doped into poly(methyl methacrylate) (PMMA) polymer thin films and incorporated into device architectures suitable for measuring transient and/or alternating electric fields (see Supplementary Information).

We attribute the observed SEC in ACRSA to the significant electric dipole associated with its charge-transfer state. Although organic molecules typically lack strong atomic spin-orbit coupling (SOC), a feature often deemed essential for enhancing the SEC [11], the SEC observed here is comparable in magnitude to that reported in transition-metal-based systems [16, 17, 22]. Notably, weak SOC is also associated with longer spin coherence times [23], even at elevated temperatures. This property enhances the sensitivity of electric field quantum sensing using SCRP at room temperature.

OPTICAL AND MAGNETIC PROPERTIES OF ACRSA

ACRSA has been extensively studied in the context of organic LEDs [24], specifically as an efficient thermally activated delayed fluorescence material, due to its strong reverse intersystem crossing (rISC) [25]. The molecular structure, shown in Fig. 1(a), consists of an electron-donating acridine unit and an electron-accepting anthracenone moiety, connected *via* a spiro-junction. This orthogonal arrangement results in weak coupling between the two π -systems, due to their spatial separation and limited orbital overlap. Both theoretical [26] and experimental [27] investigations have characterised the electronic structure and photophysics of ACRSA as a function of the solvent and the excitation wavelength. As highlighted in [27], upon excitation at $\lambda = 355$ nm, a vibronically-assisted optical transition occurs between the singlet (1A_1 , C_{2v} group) ground state and an excited singlet state localised on the anthracenone moiety ($^1LE(2^1A_1)_{n\pi^*}$). This is followed by a cascade of radiationless ISC processes to the localized triplet state

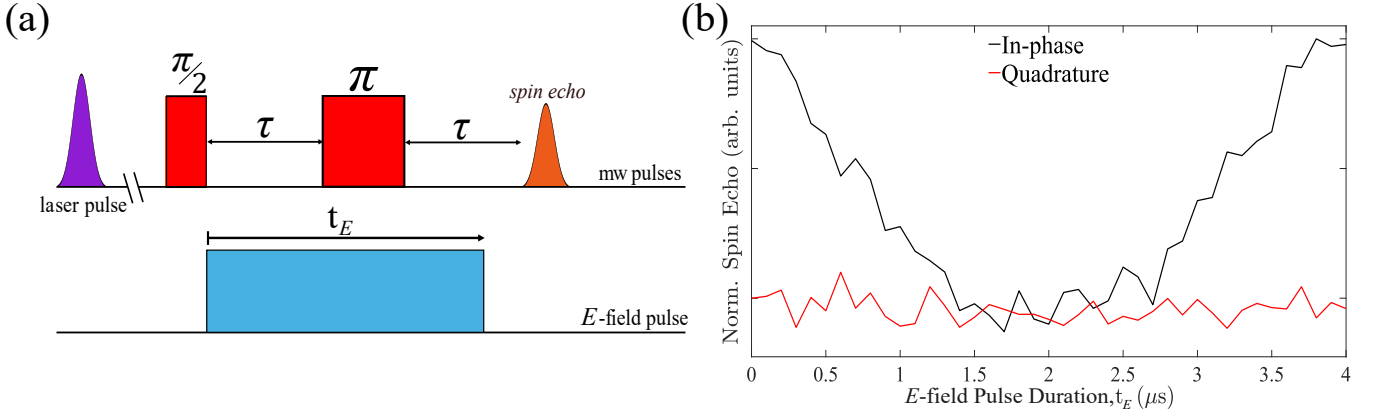


FIG. 2. (a) The modified Hahn echo sequence for SEC measurements. A laser pulse at 355 nm generates the ^3CT state with a spin-polarised initial population. After a fixed delay, a Hahn-echo sequence measures the spin coherence of the ^3CT state. An E -field pulse is inserted immediately after the $\pi/2$ microwave pulse and the echo signal is recorded as a function of the duration and/or amplitude of the E -field pulse. (b) The echo intensity as a function of the E -field pulse duration, t_E . The data were recorded at 20 K with $\tau = 2 \mu\text{s}$ and B_0 at the “Int.” field-position (as indicated in Fig. 1(c)) with an E -field of $1.5 \times 10^6 \text{ V/m}$. The absence of an electric field response in the quadrature channel arises from the combination of a linear spin–electric coupling and the random orientation of spins within the ensemble.

($^3\text{LE}(1^3\text{A}_2)_{\text{A}\pi\pi^*}$), which then undergoes internal conversion to a charge-transfer triplet state ($^3\text{CT}(2^3\text{A}_2)_{\pi\pi^*}$). A summary of these processes is shown in the Jablonski diagram in Fig. 1(d).

Fig. 1(b) shows the spin distribution of the photogenerated electron-hole pair, as calculated with DFT in the B3LYP/EPR-II basis using the ORCA software [28]. The blue surface denotes the lower energy singly occupied molecular orbital (SOMO), representing the hole density, while the red surface represents the higher SOMO. Importantly, this electron-hole pair gives rise to both a charge and a spin separation. The former results in an electric dipole moment \mathbf{p} (~ 23 Debye from the DFT calculations), while the latter leads to a zero-field splitting in the spin states characterised by an (almost perfectly) axially symmetric \mathbf{D} tensor. Both \mathbf{p} and the magnetic anisotropy axis (assuming a uniaxial symmetry) are predicted to be closely aligned with the molecular z -axis, defined as the direction connecting the nitrogen and the oxygen atoms in the molecular structure, as shown in Fig. 1(b). It is important to highlight that \mathbf{p} and \mathbf{D} both depend on the electron-hole pair wavefunction, providing an essential link between the magnetic and the electric degrees of freedom in this molecule.

Fig. 1(c, solid line) shows the echo-detected field-swept (EDFS) ESR spectrum measured on an ensemble of randomly oriented ACRSA diluted in a matrix of PMMA at 20 K, following $\lambda = 355 \text{ nm}$ excitation. The EDFS spectrum of the ^3CT state can be simulated using the EasySpin software package [29] with the following spin Hamiltonian

$$\hat{\mathcal{H}} = D(\hat{S}_z^2 - S(S+1)/3) + \mu_B g_e \mathbf{B}_0 \cdot \hat{\mathbf{S}}, \quad (1)$$

with $S = 1$, an isotropic $g_e = 2.0$ and a uniaxial anisotropy of $|D| = 317 \pm 12 \text{ MHz}$. Assuming an easy-plane type anisotropy with $D > 0$ (in agreement with DFT calculations), the simulation suggests the light-induced initial state at zero field is $\sim 100\%$ $|m_s = 0\rangle$. The combination of ESR data and DFT simulations suggests that the magnetic anisotropy of the ^3CT state arises from the magnetic dipole interaction between the spatially separated electron-hole pair, with negligible contribution from atomic SOC. This is expected in organic molecules without heavy atoms in their structure, as in the case of ACRSA [30].

To assess the coherence properties of the ^3CT state, we measured the temperature dependence of the ACRSA electron spin phase-memory time T_{2e} , as shown in Fig. 1(e). At liquid nitrogen temperature, the molecule exhibits a T_{2e} of approximately $1 \mu\text{s}$. As the temperature decreases, T_{2e} increases steadily, eventually saturating at about $2.5 \mu\text{s}$ at $T = 20 \text{ K}$. In comparison, the lifetime of the light-induced ^3CT state at 20 K exceeds $15 \mu\text{s}$ (see Supplementary Information), significantly longer than the observed spin coherence time. This indicates that the triplet-state lifetime does not constrain the spin dynamics.

Because the magnetic anisotropy (D) of the light-induced state is directly related to the dipole interaction between the electron and hole, we anticipate an external electric field to modulate D *via* coupling to the molecular electric dipole (\mathbf{p}). More precisely, owing to the lack of inversion symmetry for the electronic structure of the light-induced state, a linear SEC effect is expected to first order, that is, the E -field-induced modulation of D , $\delta D(E)$, is given

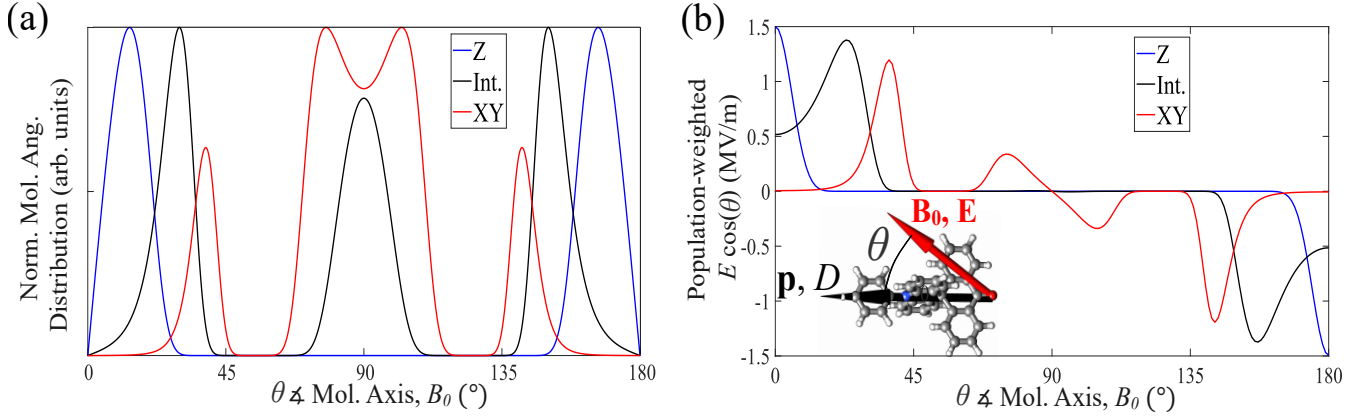


FIG. 3. (a) (Simulated) Normalized angular distribution of resonant molecules as a function of the angle θ between the external magnetic field \mathbf{B}_0 and the molecular dipole/orientation axis \mathbf{p}/D , as illustrated in the inset of panel (b). The three distributions correspond to the magnetic-field values used in the SEC study (see Fig. 1(c)). The observed peaks in the XY and Int. distributions arise from the angular dependence of the resonant field, as detailed in the Supplementary Information. (b) (Simulated) Effective electric field, calculated as the projection of the electric field along the \mathbf{p}/D axis ($E \cdot \cos(\theta)$, with $E = 1.5$ MV/m) weighted by the \mathbf{B}_0 -dependent molecular population shown in (a). This represents the strength of the interaction between the electric field and the molecular ensemble, which takes into account the angular distribution variations at different B_0 .

by

$$\delta D(E) = \kappa E \cdot \cos(\theta), \quad (2)$$

where E is the external E -field, κ is the SEC coupling coefficient and θ represents the angle between the external E -field and \mathbf{p} . To simplify the model, we make the approximation that both \mathbf{D} and \mathbf{p} are collinear with the molecular z -axis. We test this hypothesis by measuring the E -field-induced modulation of the spin echo signal in pulsed ESR experiments.

RESULTS AND DISCUSSION

We investigated the SEC in ACRSA using the modified Hahn echo sequence in Fig. 2(a), comprising an initial laser pulse at a wavelength of 355 nm which generates the ^3CT , followed by a Hahn-echo sequence measuring the spin echo signal. A square DC E -field pulse is applied immediately after the $\pi/2$ microwave pulse and the echo signal is recorded as a function of the duration/amplitude of the E -field pulse.

Representative data are shown in Fig. 2(b), where the integrated echo is plotted as a function of the E -field pulse duration. The measurement was conducted at X-band at a temperature of 20 K with a pulse length of $\tau = 2 \mu\text{s}$, under a static magnetic field of $B_0 = 340$ mT (corresponding to the “Int.” position in Fig. 4(c)). An electric field of 1.5×10^6 V/m was applied parallel to \mathbf{B}_0 . The data show a coherent SEC for the photo-excited state of ACRSA, with the in-phase component of the echo signal decreasing as the duration of the E -field pulse increases

from 0 to τ . The echo signal subsequently recovers as the duration of the E -field pulse increases from τ to 2τ , confirming a coherent SEC. On the other hand, the quadrature component of the echo signal remains at zero, independent of the E -field pulse duration. The lack of E -field response in the quadrature channel is due to the combination of a linear SEC and the sample being a randomly oriented spin ensemble [16].

To verify our hypothesis for the form of the SEC in ACRSA (Eqn. 2), we measured the E -field sensitivity for distinct ESR transitions between well defined quantum states, and we varied the orientation of the E -field against the molecular orientation [11]. This can be achieved in randomly oriented molecular ensembles by varying the strength of the static magnetic field B_0 , while keeping the ESR frequency fixed. This approach allows for the selection of a subpopulation of molecules with a specific orientation relative to \mathbf{B}_0 , due to the molecule’s uniaxial anisotropy D . Fig. 1(c) shows the three magnetic fields selected for investigation of the SEC, where B_0 is (nominally) parallel to (Z), 45° away from (Int.), and perpendicular to (XY) the molecular magnetic anisotropy axis. The simulated orientation distribution and the effective electric field for the molecules excited in the ESR experiments at each of these B_0 values are shown in Fig. 3(a, b). The latter is computed as the projection of the electric field along the \mathbf{p}/D axis ($E \cdot \cos(\theta)$, see inset in panel (b)) weighted by the \mathbf{B}_0 -dependent molecular population. Such distribution is broadened due to the presence of a sizable D strain (~ 100 MHz). Nevertheless, the simulations suggest a good orientation selection in the ESR experiments. The presence of three peaks in the XY and Int. distri-

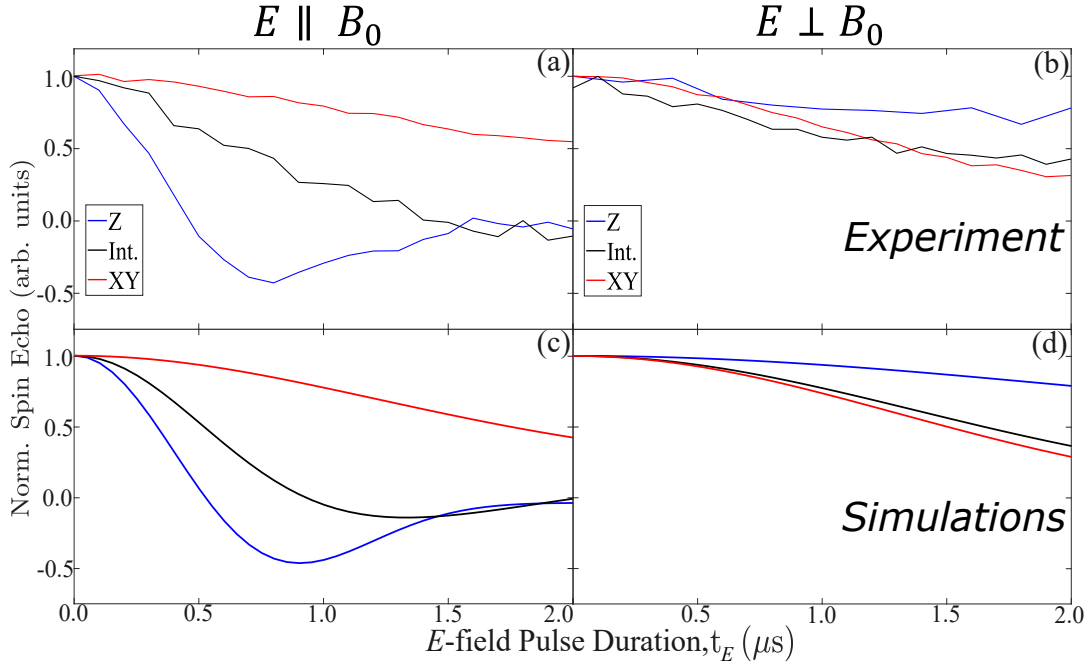


FIG. 4. (a-b) Integrated spin-echo intensity as a function of the electric-field pulse duration varied from 0 μs to τ ($= 2 \mu\text{s}$), for the three field positions considered in the study (see insets). The two configurations correspond to the electric field being parallel (left) and perpendicular (right) to \mathbf{B}_0 . In the parallel configuration, the most pronounced electric modulation occurs at Z, while in the perpendicular configuration, it occurs at XY. These positions correspond to the largest alignment between the electric dipole moment/ D and the applied E -field, supporting the model in which D is the primary contribution to the electric modulation. (c-d) Simulations of the electric-field modulation for (a-b), respectively. The model assumes that D is the only spin Hamiltonian term modulated by the electric field. This modulation is described by $D(E) = D(0) + \kappa E \cdot \cos(\theta)$, where θ is the angle between D and the applied E -field. The coupling strength, $\kappa = 1.45 \text{ Hz}/(\text{V}/\text{m})$, quantifies the interaction between the E -field and the magnetic anisotropy.

butions is a consequence of the resonance-field angular dependence in ACRSA, whose details are shown in the Supplementary Information.

The experimental results are shown in Fig. 4(a,b), with simulations based on our simple model shown in Fig. 4(c,d). Overall, the SEC effect is strongest when the E -field and \mathbf{B}_0 are both parallel to the molecular D axis (Fig. 4(a), blue trace); this is the configuration in which the E -field couples most strongly to the molecular electric dipole \mathbf{p} , and in which the spin transition energies are most sensitive to a change in the magnitude of D . The strength of the SEC decreases as the E -field makes a greater angle with the molecular dipole moment \mathbf{p} (i.e., the electric coupling energy decreases), as well as when \mathbf{B}_0 moves away from the anisotropy axis, that is, when the magnetic field induces mixing between spin states aligned with and deviating from the molecular anisotropy axis.

The maximum observed E -field sensitivity of the ESR transition, $\delta f = (1.20 \pm 0.05) \text{ Hz}/(\text{V}/\text{m})$, is comparable to those reported for transition metal-based molecular nanomagnets [16, 17, 22]. This is despite the spin density residing in the π -system of a molecule with

light elements (p -orbitals) with negligible atomic SOC, highlighting the importance of the significant molecular electric dipole in facilitating SECs. The results can be explained quantitatively with a SEC coefficient of $\kappa = (1.45 \pm 0.1) \text{ Hz}/(\text{V}/\text{m})$. A strain of this coefficient ($\sigma_\kappa = (0.70 \pm 0.02) \text{ Hz}/(\text{V}/\text{m})$) was also applied in the simulations, which, together with the orientation distribution of the molecules, explain the shapes of the echo intensity vs. E -field pulse shown in Fig. 4(a) and (c).

The SEC model is further verified by applying the E -field perpendicular to the static magnetic field B_0 . The ESR spectrum is unchanged due to the random orientation nature of the sample. By contrast, the relative alignment between the E -field and the molecular electric dipoles is altered in this configuration, leading to different SEC effects. For instance, when measuring the SEC effect with B_0 at the Z field position (Fig. 4(b)), the E -field is mostly perpendicular to the molecular z -axis, i.e. to its electric dipole \mathbf{p} . Hence, unlike the $E \parallel B_0$ configuration, in which the strongest SEC effect is observed with B_0 at the Z field position, the ESR transition is almost insensitive to the E -field at the same B_0 with $E \perp B_0$. This behaviour is quantitatively reproduced by the simulations shown in Fig. 4(d), which employ the same model

and parameters as those used for the $E \parallel B_0$ configuration. This provides further support for our SEC model. Finally, it is noteworthy that the SEC analysis is not affected by the sign of D . Fitting the ESR spectrum and the SEC measurements with $D < 0$ leads to similar conclusions for the SEC (see Supplementary Information).

CONCLUSION AND FUTURE WORK

By studying the SEC in a light-induced spin-polarised charge-transfer state in ACRSA, we show that the substantial electric dipole moment associated with the CT state enables coupling between the molecular spin and an external electric field. This finding demonstrates that a sizable SEC can be achieved *via* spin-spin interactions alone, with negligible contribution from atomic SOC. Future work will explore the structure-property relations with the aim of optimizing the SEC response for the design of more sensitive quantum devices.

The two major constraints to the sensitivity of the current device are the random molecular orientation and the relatively short spin coherence time, which restricts sensing applications to cryogenic temperatures. These limitations could be mitigated by aligning the molecules using magnetic fields [31], employing magnetic dilution [32], and deuterating [14, 33] or applying mechanical strains to the host polymer matrix [34]. Together with the capability for optical spin state initialization, such strategies could significantly enhance sensitivity and enable room-temperature operation.

Furthermore, recent advances in optical spin detection of molecular nanomagnets [10, 35] pave the way for room-temperature electric field sensing using miniaturized spintronic devices incorporating just a few, or even single, molecules. Finally, by exploiting spin-correlated radical pairs with substantial SOC, the molecular SEC can be enhanced to levels comparable to, or exceeding, those reported for some transition-metal- and lanthanide-based molecules, further boosting electric field sensitivity.

[1] C. Degen *et al.*, Quantum sensing, *Rev. Mod. Phys.* **89**, 035002 (2017).
 [2] Z. Qiu *et al.*, Nuclear spin assisted magnetic field angle sensing, *npj Quantum Inf.* **7**, 39 (2021).
 [3] M. Bal *et al.*, Ultrasensitive magnetic field detection using a single artificial atom., *Nat. Commun.* **3**, 1324 (2012).
 [4] D. Schäffner, T. Schreiber, F. Lenz, M. Schlosser, and G. Birkel, Quantum sensing in tweezer arrays: Optical magnetometry on an individual-atom sensor grid, *PRX Quantum* **5**, 010311 (2024).
 [5] C. Fancher *et al.*, Rydberg atom electric field sensors

for communications and sensing, *IEEE Transactions on Quantum Engineering* **2**, 3501313 (2020).
 [6] J. Yoo *et al.*, Trapped-ion based nanoscale quantum sensing, *Nano Convergence* **12**, 12 (2025).
 [7] S. Danilin *et al.*, Quantum sensing with tunable superconducting qubits: optimization and speed-up, *New J. Phys.* **26**, 103029 (2024).
 [8] C.-J. Yu *et al.*, A molecular approach to quantum sensing, *ACS Cent. Sci.* **7**, 712–723 (2021).
 [9] F. Troiani *et al.*, Towards quantum sensing with molecular spins, *Journal of Magnetism and Magnetic Materials* **491**, 165534 (2019).
 [10] K. R. Mullin *et al.*, Quantum sensing of magnetic fields with molecular color centers, *Phys. Rev. Res.* **5**, L042023 (2023).
 [11] J. Liu *et al.*, Quantum coherent spin-electric control in molecular nanomagnet at clock transitions, *Nature Physics* **17**, 1205 (2021).
 [12] W. W. and B. Liu, Modulating the optical properties and functions of organic molecules through polymerization, *Materials Horizons* **9**, 99 (2022).
 [13] S. Saha *et al.*, From molecules to interactions to crystal engineering: Mechanical properties of organic solids, *Accounts of Chemical Research* **11**, , 2957–2967 (2018).
 [14] J. M. Zadrozny *et al.*, Millisecond coherence time in a tunable molecular electronic spin qubit, *ACS Cent. Sci.* **1**, 488 (2015).
 [15] M. Wasielewski *et al.*, Exploiting chemistry and molecular systems for quantum information science, *Nature Reviews Chemistry* **4**, 490 (2020).
 [16] J. Liu *et al.*, Electric field control of spins in molecular magnets, *Phys. Rev. Lett.* **122**, 037202 (2019).
 [17] Y.-H. Fang *et al.*, Spin-electric coupling with anisotropy-induced vanishment and enhancement in molecular ferroelectrics, *JACS* **144**, 19 (2022).
 [18] W. M. Harvey, S.M., Photogenerated spin-correlated radical pairs: From photosynthetic energy transduction to quantum information science, *J. Am. Chem. Soc.* **38**, 15508–15529 (2021).
 [19] B. Rugg *et al.*, Photodriven quantum teleportation of an electron spin state in a covalent donor–acceptor–radical system, *Nat. Chem.* **11**, 981–986 (2019).
 [20] F. Xie *et al.*, Quantum sensing of electric fields using spin-correlated radical ion pairs, *J. Am. Chem. Soc.* **27**, 14922–14931 (2023).
 [21] W. Mims, *The Linear Electric Field Effect in Paramagnetic Resonance* (Clarendon Press, Oxford, 1976).
 [22] R. E. George *et al.*, Coherent spin control by electrical manipulation of the magnetic anisotropy, *Phys. Rev. Lett.* **110**, 027601 (2013).
 [23] M. Fittipaldi *et al.*, Electric field modulation of magnetic exchange in molecular helices, *Nat. Mater.* **18**, 329 (2019).
 [24] K. Stavrou *et al.*, Key requirements for ultraefficient sensitization in hyperfluorescence organic light-emitting diodes, *Nat. Photon.* **18**, 554–561 (2024).
 [25] L. Franca *et al.*, Spiro donor–acceptor tadf emitters: naked tadf free from inhomogeneity caused by donor acceptor bridge bond disorder. fast rise and invariant photophysics in solid state hosts, *J. Mater. Chem. C* **10**, 1313 (2022).
 [26] I. Lyskov and C. M. Maryan, Climbing up the ladder: Intermediate triplet states promote the reverse intersystem crossing in the efficient tadf emitter acrsa, *J. Phys.*

- Chem. C **121**, 21145–21153 (2017).
- [27] L. G. Franca *et al.*, Donor, acceptor, and molecular charge transfer emission all in one molecule, A. Phys. Chem. Lett. **14**, 2764–2771 (2023).
- [28] F. Neese *et al.*, The orca quantum chemistry program package, J. Chem. Phys. **152**, 224108 (2020).
- [29] S. Stoll and A. Schweiger, Easyspin, a comprehensive software package for spectral simulation and analysis in epr, J. Magnetic Resonance **178**, 42 (2006).
- [30] G. Moise *et al.*, The impact of spin–orbit coupling on fine-structure and spin polarisation in photoexcited porphyrin triplet states, Journal of Magnetic Resonance **355**, 107546 (2023).
- [31] M. Boamfa *et al.*, Magnetic field alignment of liquid crystals for fast display applications, Advanced Materials **17** (5), 610 (2005).
- [32] C. E. Jackson *et al.*, A reaction-coordinate perspective of magnetic relaxation, Chem. Soc. Rev. **50**, 6684 (2021).
- [33] A. Arzhang *et al.*, Will spin-relaxation times in molecular magnets permit quantum information processing?, Phys. Rev. Lett. **98**, 057201 (2007).
- [34] G. Stoclet *et al.*, Strain-induced molecular ordering in polylactide upon uniaxial stretching, Macromolecules **43** (3), 1488 (2010).
- [35] D. Laorenza *et al.*, Tunable Cr⁴⁺ molecular color centers, JACS **143**, 21350–21363 (2021).

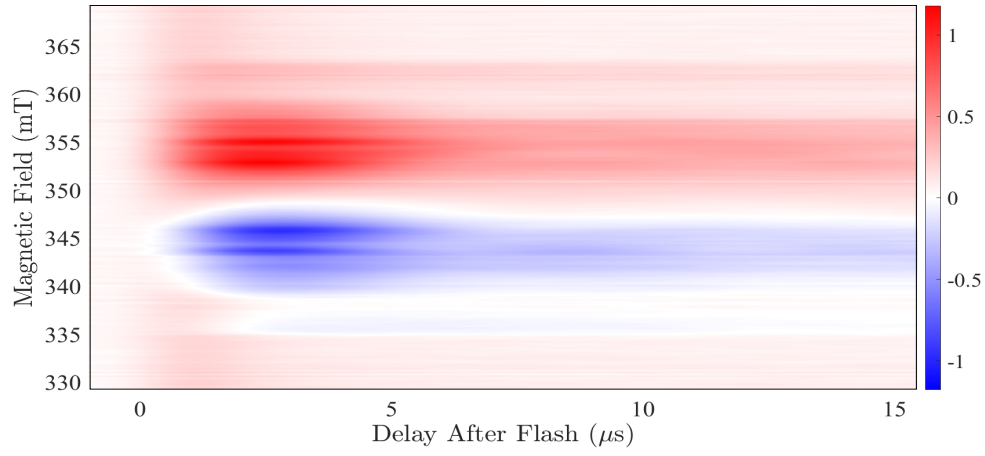


FIG. S1. The ESR spectrum of a 5% solution of ACRSA doped in PMMA, measured at 20 K under 355 nm photoexcitation as a function of time after the laser pulse (known as delay after flash). This reveals a long-lived triplet state with a lifetime exceeding 15 μs , which is significantly longer than the electron spin-phase memory time at the same temperature ($\sim 2.5 \mu\text{s}$, see the main text). Thus, the triplet-state lifetime of the charge-transfer state does not interfere with the sensing protocol proposed in the study. The blue (red) areas indicates the emission (absorption) part of the spectrum.

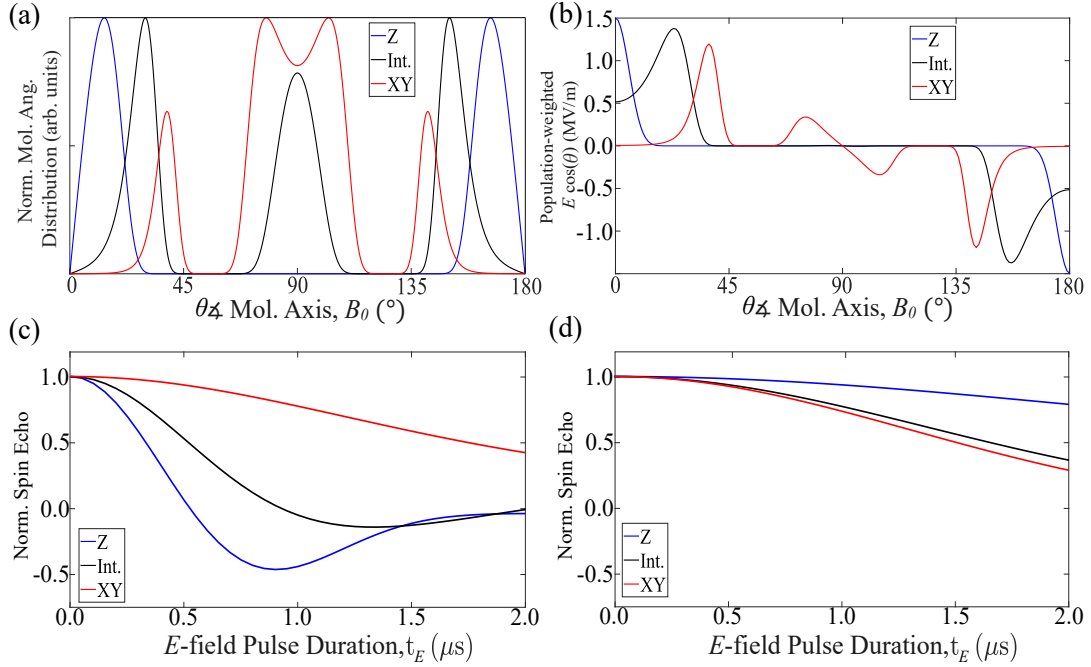


FIG. S2. The simulations for (a) the angular distribution, (b) the effective electric coupling, and the electric modulations for (c) $E \parallel B_0$ and (d) $E \perp B_0$ were repeated with the sign of the magnetic anisotropy parameter D reversed (i.e., $D < 0$). These simulations yielded results indistinguishable from those presented in the main text, indicating that the spin-electric-coupling model is insensitive to the sign of D .

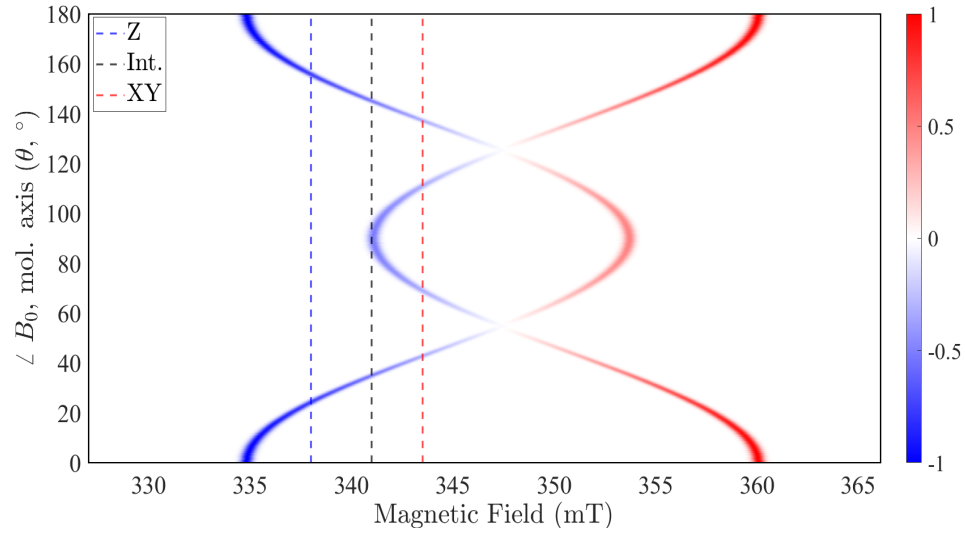


FIG. S3. The figure shows the resonance fields for ESR emission (blue) and absorption (red) transitions as a function of the angle θ between the molecular axis and the static magnetic field B_0 . The three vertical dashed lines indicate the specific field positions where we performed spin-electric coupling measurements in ACRSA. By extracting cross-sections at these field values, we obtained the simulated molecular-orientation distributions shown in the main text, which in turn explain the presence of the three-peak structure observed in the angular distributions at the XY and Int. field positions.

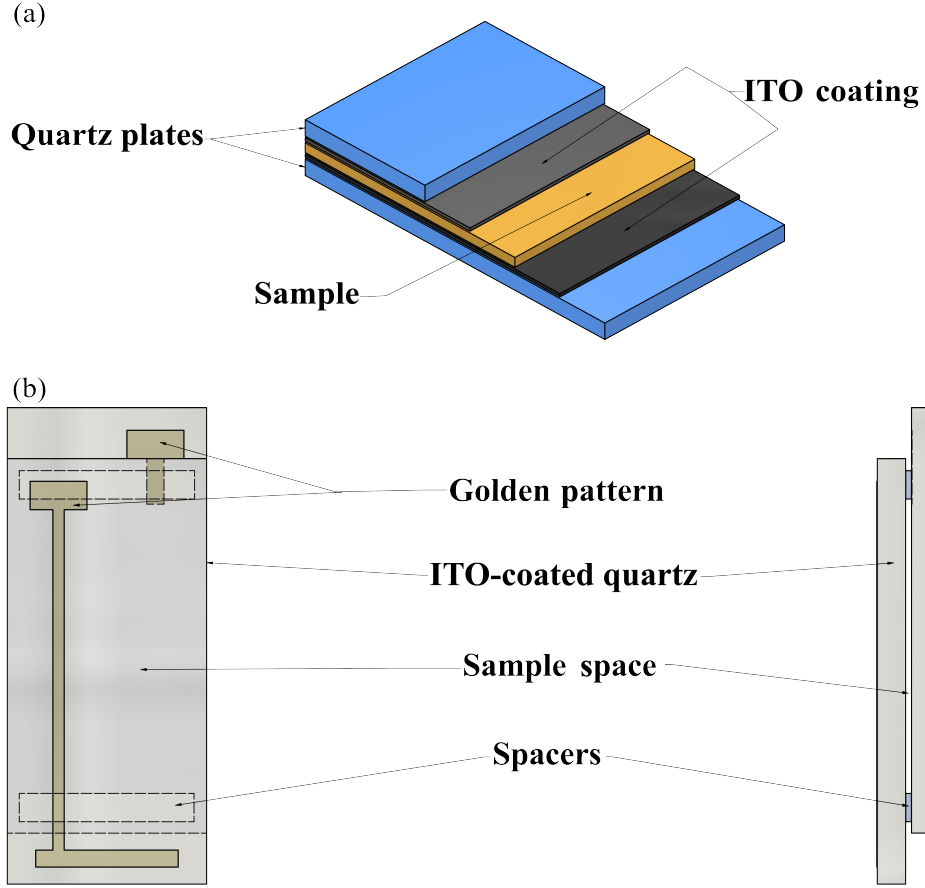


FIG. S4. (a) A false-colour scheme of the E -field device used in the measurements. The DC electric-field pulse is generated by applying a voltage across a parallel-plate capacitor, whose electrodes are made from quartz coated with indium-tin oxide. These electrodes are nearly perfectly transparent to UV and microwave excitations, thus allowing both the initial laser and ESR pulses to interact with the sample. (b) A more detailed schematic of the device, illustrating the T-shaped golden patterns and the offset between the two plates. These features ensure multiple wire bondings between the device and the E -field supply. With the pulse intensity set to 300 V and the separation between the two capacitor plates roughly equal to $200\ \mu\text{m}$, an electric field of approximately $\sim 10^6\ \text{V/m}$ is generated at the sample site.

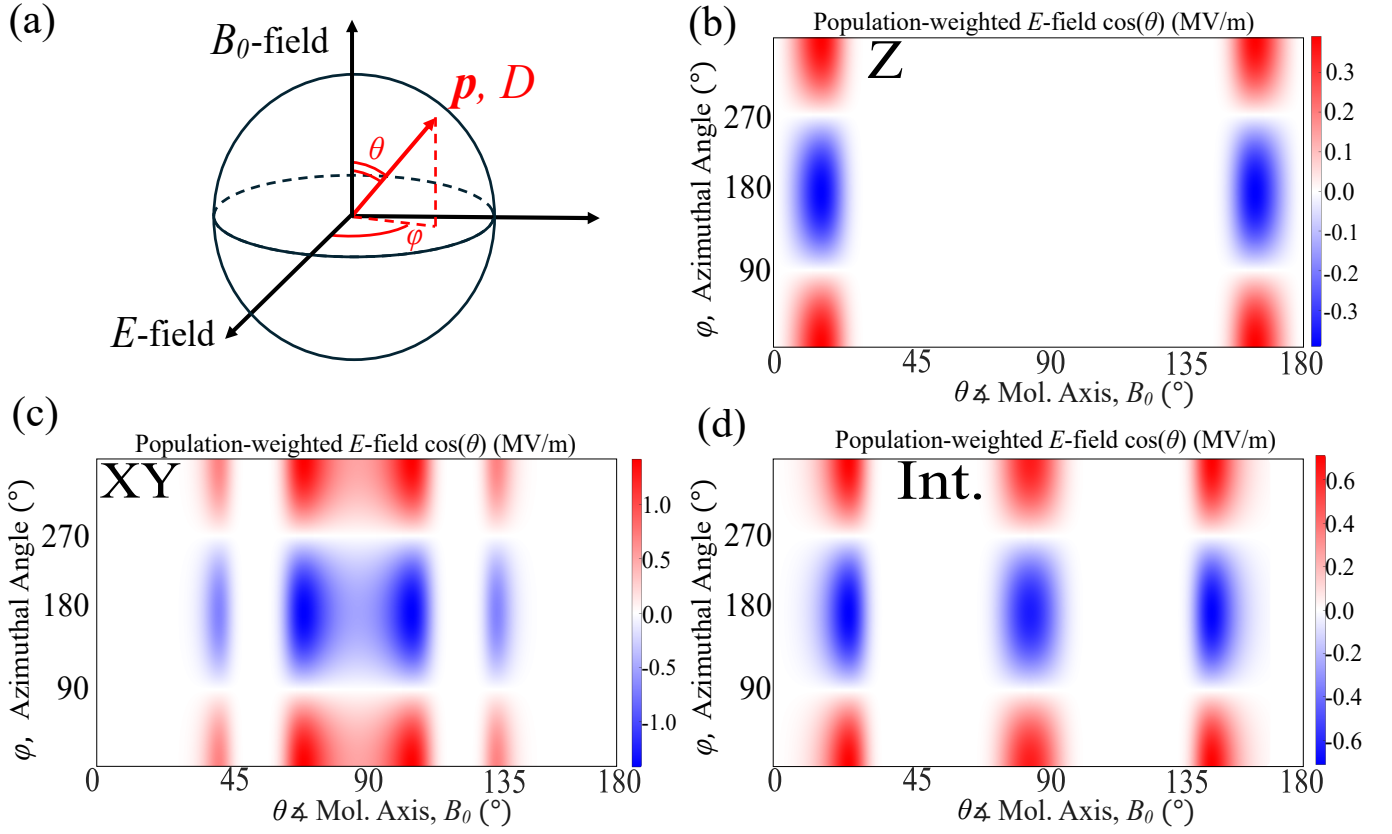


FIG. S5. Schematic illustration of the molecular orientation (red arrow), with the molecular axis labeled as “ D, \mathbf{p} ”, in the configuration $E \perp B_0$. In contrast to the $E \parallel B_0$ case discussed in the main text, the angle between the E -field and the molecular axis (determining the strength of the spin-electric coupling) depends on both the polar angle θ between the molecular axis and B_0 , and the azimuthal angle φ between the plane spanned by $\{E, B_0\}$ and the molecular axis. (b-d) Angular dependence of the population-weighted effective E -field (in MV/m) for three field positions: Z (b), XY (c), and Int. (d).